Causa, F., et al. (2019). Runaway electron imaging spectrometry (REIS) system. *Review of Scentific instruments*, 90(7): 073501, [9] p.

Runaway electron imaging spectrometry (REIS) system

View Online   Export Citation   CrossMark

F. Causa,[1,a] M. Gospodarczyk,[2] P. Buratti,[3] D. Carnevale,[4] R. De Angelis,[3] B. Esposito,[3] A. Grosso,[3]
G. Maddaluno,[3] J. R. Martin-Solis,[5] V. Piergotti,[3] Z. Popovic,[5] G. Rocchi,[3] A. Sibio,[3] C. Sozzi,[1] B. Tilia,[3]
M. Valisa,[6] and FTU Team[3,b]

AFFILIATIONS

[1] Istituto di Fisica del Plasma, Consiglio Nazionale delle Ricerche, Via R. Cozzi, 53, 20125 Milano, Italy

[2] INFN, Laboratori Nazionali di Frascati, Via E. Fermi 40, 00044 Frascati, Italy

[3] ENEA, Dipartimento FSN, C. R. Frascati, Via E. Fermi 45, 00044 Frascati (Roma), Italy

[4] Dip. di Ing. Civile e Ing. Informatica, Università di Roma, Tor Vergata, 00133 Roma, Italy

[5] Universidad Carlos III de Madrid, Avda. Universidad 30, Leganes 28911, Madrid, Spain

[6] Istituto Gas Ionizzati, Consiglio Nazionale delle Ricerche, Consorzio RFX, Corso Stati Uniti, 4, 35127 Padova, Italy

[a] Electronic mail: causa@ifp.cnr.it
[b] See the appendix of G. Pucella *et al.*, Proceedings of the 27th IAEA Fusion Energy Conference, Gandhinagar, India, 2018.

ABSTRACT

A portable Runaway Electron Imaging and Spectrometry System (REIS) was developed in ENEA-Frascati to measure synchrotron radiation spectra from in-flight runaway electrons in tokamaks. The REIS is a wide-angle optical system collecting simultaneously visible and infrared emission spectra using an incoherent bundle of fibers, in a spectral range that spans from 500 nm to 2500 nm, and visible images using a CCD color microcamera at a rate of 25 frames/s. The REIS system is supervised and managed using a dedicated LabVIEW program to acquire data simultaneously from three spectrometers every 20 ms (configurable down to 10 ms). An overview of the REIS architecture and acquisition system and resulting experimental data obtained in FTU are presented and discussed in this paper.

Published under license by AIP Publishing. https://doi.org/10.1063/1.5061833

I. INTRODUCTION

Runaway Electrons (REs) are beams of electrons accelerated to velocities close to the speed of light. They represent a major concern in tokamaks because when they are lost to the first wall, significant local energy deposition, local melting, and damage of plasma-facing components may occur.[1] Key to the successful operation of tokamaks and, in particular, of ITER and future energy-generation reactors of the DEMO type is the ability to control REs to mitigate their impact on machine operation. Such issues can be studied in detail in dedicated programs in smaller experiments that permit the realization of relevant scenarios involving significant fractions of REs.[2–4] In this context, the recent integration of different diagnostics[5] and new software tools within the FTU real-time RE control system[6,7] is contributing to the characterization of RE dynamics[8] to the study of effective mitigation strategies[9] and to the design of control-oriented dynamical models of current, horizontal, and vertical displacement for REs in the postdisruption phase.[10]

A specific activity was focused on the design, development, and construction of a new plasma diagnostic, referred to as REIS (RE Imaging and Spectroscopy system) to detect and study in-flight REs. Synchrotron radiation measurements using imaging and spectral analysis provide a tool to detect the presence of REs when they are still confined within the plasma and to deduce their energy from measured spectra and an assumed pitch angle. The REIS is intended to provide indirect information on the RE energy distribution function in the various phases of a discharge, particularly during RE plateaus following disruption events in which a large part of the plasma current is carried by relativistic electron beams.

Although synchrotron imaging RE diagnostics are widely used in present-day tokamaks (see for an overview[11–17]), there are two

main novelties in the REIS prototype system described here: (a) it permits the simultaneous detection of visible (VIS) and near infrared (NIR) spectra of synchrotron radiation and (b) it is designed to be portable to other medium size tokamaks, such as AUG and TCV.

The paper is organized as follows: after a brief introduction on synchrotron radiation measurements in tokamaks provided below in this section, the REIS diagnostic and its setup in FTU are described in Sec. II, together with the calibration procedure and software architecture. Experimental results and the energy estimation procedure in FTU runaway discharges are presented in Sec. III. Finally, Sec. III draws some conclusions and gives some information about future work. Note that results obtained with the REIS in AUG and TCV will be presented elsewhere, but recent developments on RE studies in these devices can be found in Ref. 18.

Synchrotron radiation is emitted by charged particles moving at relativistic speeds in magnetic fields. When the electron speed approaches that of light, the emission pattern is directed in a narrow beam in the direction of motion of the electron. The emission power depends on electron energy, pitch angle, and magnetic field intensity, thus making it possible to estimate the most important RE parameters, namely, pitch angle θ, beam radius, maximum energy, and current, from calibrated spectra and images.

The brightness of the measured synchrotron radiation can be expressed, as done in Refs. 19 and 20, as

$$B_r(\lambda, \theta, \gamma) = P(\lambda, \theta, \gamma) \frac{2R}{\pi\theta} n_{RE}, \tag{1}$$

where n_{RE} is the density of the observed REs, R is the torus major radius, θ the pitch angle, and $P(\lambda, \theta, \gamma)$ is the synchrotron power spectrum emitted by a single runaway electron. The synchrotron power spectrum, in cylindrical approximation, can be expressed as[20]

$$P_{cyl}(\lambda, \theta, \gamma) = \frac{ce^2}{\sqrt{3}\epsilon_0 \lambda^3 \gamma^2} \int_{\lambda_c/\lambda}^{\inf} K_{5/3}(l)dl, \tag{2}$$

where e is the electron charge, c is the speed of light, ϵ_0 is the vacuum permittivity, $K_v(x)$ is the modified Bessel function of second kind, γ is the relativistic factor, λ is the wavelength, and λ_c is a critical wavelength expressed by

$$\lambda_c = \frac{4\pi}{3} \frac{cm_e \gamma_{||}}{eB\gamma^2}, \tag{3}$$

with m_e being the electron rest mass and $\gamma_{||} = (1 - v_{||}^2/c^2)^{-0.5}$ being the relativistic factor corresponding to the motion parallel to the magnetic field B. The cylindrical approximation is valid only for small pitch angles and does not take into account the effects of magnetic field line curvature and curvature drift, typical of a tokamak geometry. In tokamaks, such effects have to be taken into account,[20] for a correct description of the synchrotron emission spectrum.

Synchrotron radiation spectra in tokamak devices are typically peaked in the infrared part of the spectrum.[11,14,21] Figure 1 shows the theoretical curves obtained using Eq. (1) for monoenergetic electrons in three tokamak devices with increasing
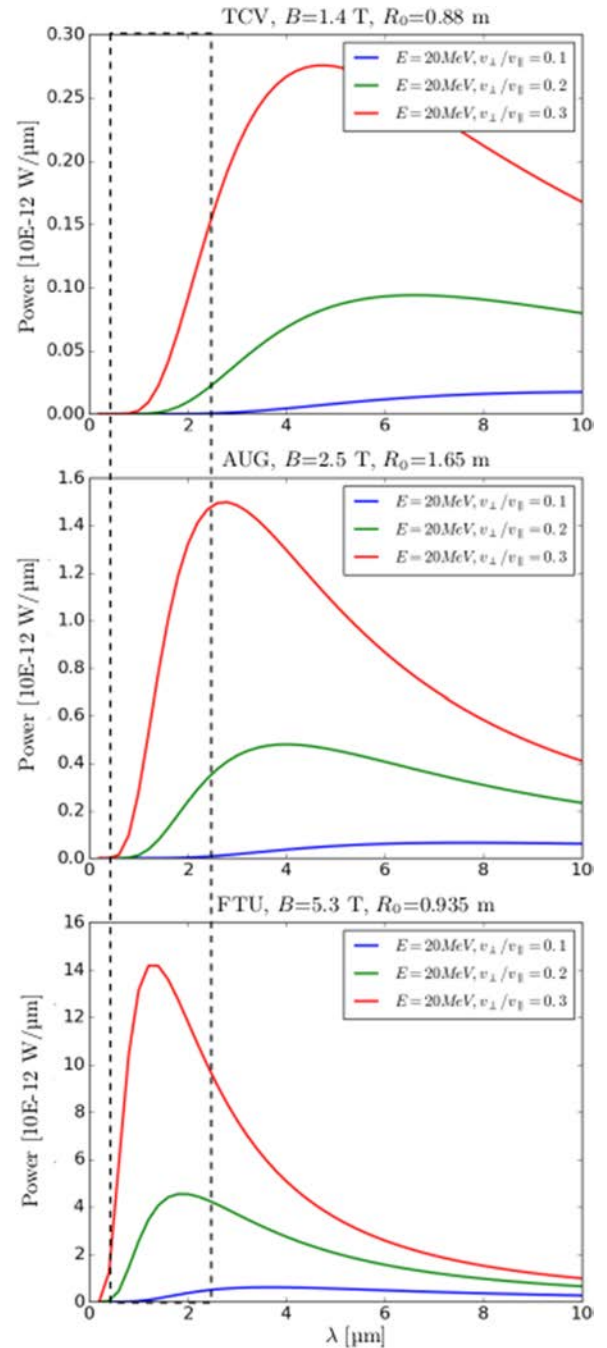

FIG. 1. Synchrotron emission spectra calculated using Eq. (1) for TCV, AUG, and FTU at different energies and different pitch angle parameters $\frac{v_{||}}{v_\perp} = \tan(\theta)$. The dashed lines show the spectral range of the present REIS diagnostic.

magnetic fields (from the top: TCV, AUG, and FTU). The spectra presented in Fig. 1 demonstrate the importance of detecting synchrotron spectra in the infrared to capture a significant part of the curve to improve data interpretation capability.
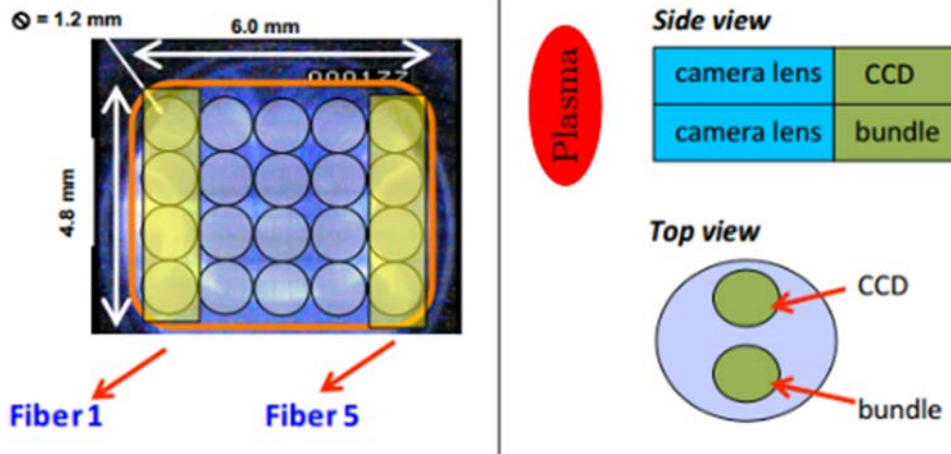
FIG. 2. (right) REIS head including one CCD camera and one fiber bundle, each coupled to a wide angle camera lens; (left) 5 × 4 incoherent fiber bundle overlapped with an image of the FTU vessel cross section taken with the CCD camera: the shaded regions show the image sections observed by the fibers for spectral analysis.

The REIS diagnostic was developed specifically with this purpose in mind.

II. REIS DIAGNOSTIC

A. Detection system

A schematic of the REIS diagnostic head is presented in Fig. 2 (right), while its main components are shown in Fig. 3.

A wide-angle objective lens (f = 3 mm) is coupled to a visible CCD camera (Toshiba, sensor imaging at 25 fps) to collect the visible video images of the vessel cross section comprising both in-coming (forward view) and out-going (backward view) RE directions of flight, corresponding to the two poloidal sections of the vessel. The CCD camera is characterized by a 5.5 mm × 6 mm active area.

A second identical wide-angle camera lens is coupled to an incoherent, 20-fiber bundle, arranged as an array of 5 columns of 4 low-OH optical fibers. A schematic of the incoherent bundle of 20 fibers superimposed to the cross section image of the FTU vessel is presented in Fig. 2 (left).

The fiber bundle is designed to permit five straight bare outputs of four-fiber bundles. Any of the five individual outputs can be connected to a spectrometer to detect and measure the optical spectrum of the collected radiation. The used fibers outputs correspond to the first and last columns (fiber 5 for forward viewing and fiber 1 for backward viewing); see Fig. 2 (left). They are connected to the spectrometers through a set of coupling lenses embedded in a coupling box with the dual purpose of mixing the optical signal collected via the individual fibers in each column and of providing a way to connect the bare fibers to the spectrometers. The layout of the fibers and spectrometers is provided in Fig. 4, while Fig. 5 shows the camera and spectrometers field of view (FOV) overlaying a schematic midplane cross section of FTU.

The fiber output corresponding to forward view is connected to a low-OH bifurcated fiber (Thorlabs, BFY1000LS02 Bifurcated Fiber Bundle, ø 1000 μm Core, Low OH, SMA, 2 m) and thus to a set of two spectrometers, one operating in the visible (HR2000+, Ocean Optics, Range: 190–1100 nm, CCD Line Array, 2028 pixels) and the other one in the infrared range (NIRQUEST256, Ocean Optics, Range: 900–2500 nm, CCD Line Array, 256 pixels) to permit the simultaneous detection of visible and infrared spectra of the collected synchrotron emission. The second fiber output, collecting the signal from the backward view, is connected to a single spectrometer operating in the visible range (HR2000+, Ocean Optics, Range: 190–1100 nm).

B. Software architecture

The REIS system is supervised and managed by a dedicated LabVIEW program collecting data every 20 ms (configurable down
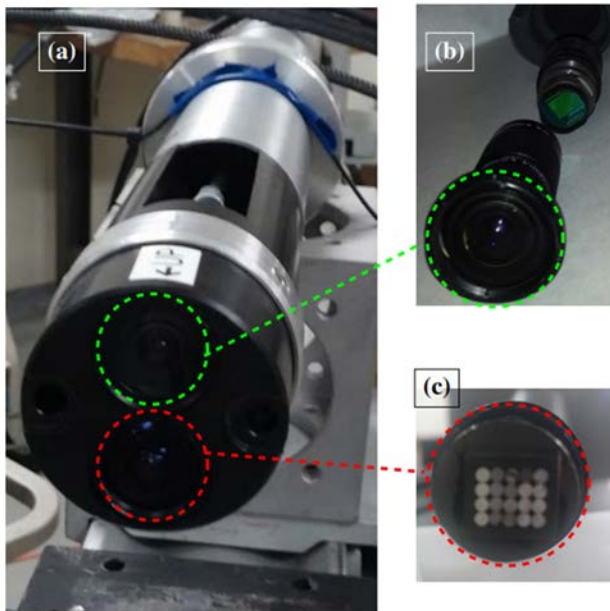

FIG. 3. REIS main optical components: (a) picture of the optical head; (b) picture of the objective lens, CCD camera, and housing (imaging); and (c) 5 × 4 incoherent fiber bundle array.
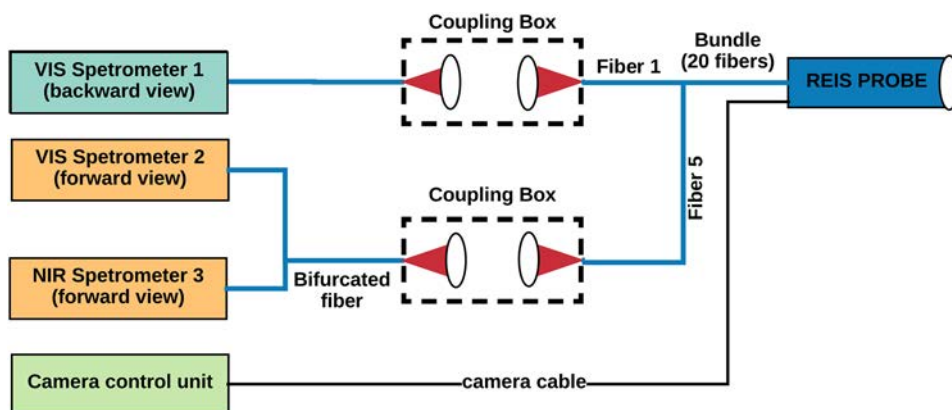
FIG. 4. Layout of fibers and spectrometers and camera control unit.

to 10 ms) simultaneously from the three spectrometers and every 40 ms from the camera. The acquisition system is synchronized with the main common gate of the tokamak. Trigger time phasing for acquisition in external hardware triggering is represented in Fig. 6. In case the collected signal is too low, it is possible to increase the integration time.

The three spectrometers are synchronized by a NI PCI-6602 (8-Channel Counter/Timer with Digital I/O) board that generates a preset number of pulses at a given frequency.

FIG. 5. Schematic of the FTU midplane cross section, showing the location of the REIS head in port 6 (P6). The camera and spectrometers field of view (FOV) are shaded, respectively, in gray and brown. The wide-angle camera is viewing both co- and counter-plasma current directions inside the tokamak, while the spectrometers have either forward view (fiber 5) or backward view to (fiber 1).

Image acquisition is performed by a NI PCI-1411 card supporting analog format. The data acquisition system runs on a dedicated personal computer (PC) using LabVIEW for easy integration in different medium sized-tokamaks. The acquisition logic is based on a state machine pattern which is one of the fundamental architectures used in LabVIEW to implement complex decision-making algorithms represented by state diagrams (Fig. 7). In the diagram, the states describe the actions that are performed when the control process is in that state, whereas the transitions (arrows) describe when and how the process can move from one state to another.

The REIS state diagram is composed of the following states:

1. INIT: this state is for the initialization, monitoring, and control of hardware/software such as device type, integration time, and number of acquisitions in accord with pulse train generator used for the control of the NI PCI-6602 board.
2. PRERUN: in this state, the REIS system awaits for the software trigger, typically starting 30 s before the beginning of the pulse (referred to as "zero plasma"). The software trigger is related to the state of a specific tokamak device, e.g., on FTU, such state is retrieved by querying a specific database every 2 s. In the software trigger state, it is also possible to retrieve the current pulse number. When the software trigger is high, then the state machine moves into the RUN state.
3. RUN: in this state, the REIS system is awaiting for the tokamak common gate to begin data acquisition. When the common gate is high, then the system starts the acquisition of spectra and images. During the acquisition, data are temporarily locally stored and then saved on the REIS PC file system. Data acquisition is synchronized with the pulse train generated by a dedicated hardware installed on the REIS PC. When the pulse train is completed and no errors occur, the state machine moves into the ENDRUN state. The tokamak common gate is specific to the device on which the REIS is installed and must be taken into account during data processing, e.g., on FTU, it starts at 50 ms before zero plasma.
4. ENDRUN: this state is dedicated to data storage on the REIS PC file system. After this, the system moves back to the PRERUN state for a new acquisition.
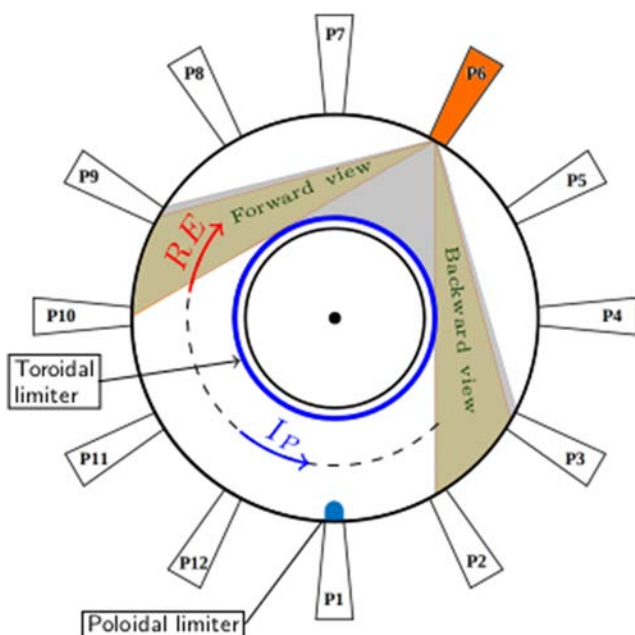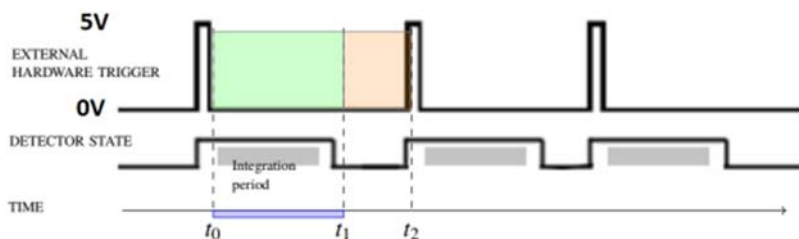
FIG. 6. Trigger timing phases. The system first cleans the memory and then starts the integration for a fixed period of time (green box). Once the integration is over, it transfers the data to the host machine and waits for the next trigger (orange box); t_0 is the acquisition time, t_1 is the integration time, and t_2 is the data transfer time (in FTU: $t_0 = 0$ ms, $t_1 = 15$ ms, and $t_2 = 20$ ms).
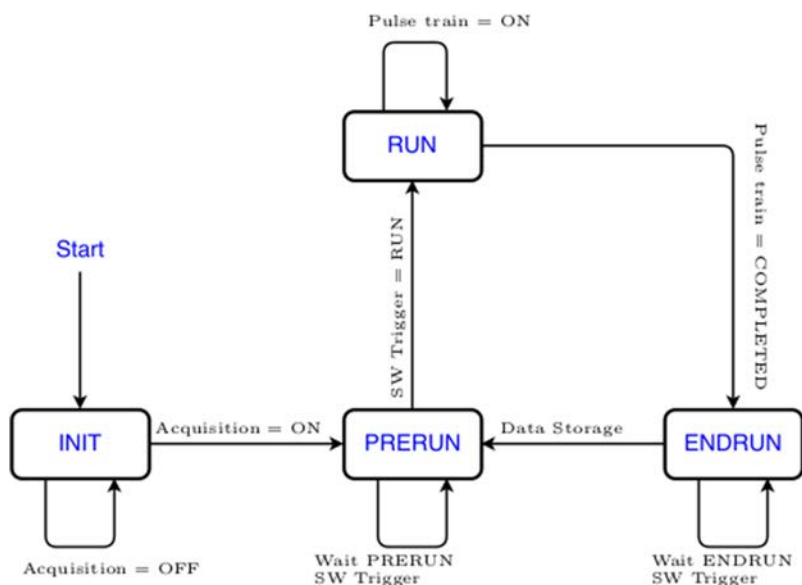

FIG. 7. REIS state diagram.

C. Calibration

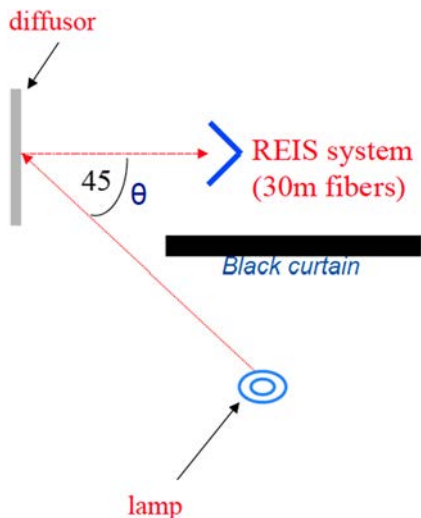The visible spectrometers were radiometrically calibrated in the laboratory using a calibrated tungsten lamp (220 A Optronic Laboratory, 200 W, 6.5 A) and a calibrated lambertian diffuser (National Physical Laboratory). The absolute calibration in the visible range was performed using the lamp-diffuser system. The calibrated lamp was placed at a distance of 50 cm from the diffuser. The diffuser was placed at an angle of 45° with respect to the lamp (Fig. 8). The calibration curve was obtained as the ratio of the radiance of the diffuser to the measured data. Since the diffuser was calibrated in the visible range, the resulting curve represents the absolute calibration curve of the system in the visible range.

However, since the calibrated output power level was lower than expected and could not be detected by the infrared spectrometer in the given configuration, a relative calibration was carried out in the infrared part of the spectrum. The lamp was pointed directly into the optical system of the REIS, at a distance of only 4 cm to detect the signal (Fig. 9). The blackbody curve describing the calibrated tungsten lamp (temperature = 1750 °C) was extrapolated up
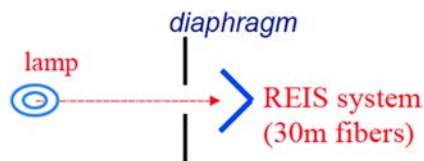

FIG. 8. Schematic setup of the absolute calibration of the visible range.

FIG. 9. Schematic setup of the relative calibration of the infrared range.
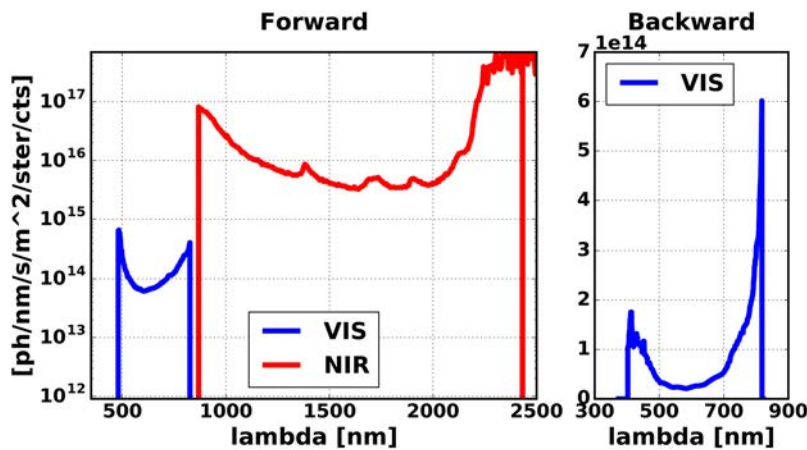
FIG. 10. Spectrometers calibration curves.

to the infrared range. The relative calibration curve was obtained as the ratio of the extrapolated blackbody curve to the measured data.

The resulting absolute visible (forward and backward) and relative infrared calibration curves are presented in Fig. 10. Calibrated synchrotron emission spectra, such as those presented in Sec. III, have been obtained by joining the absolutely calibrated spectra in the visible and the relatively calibrated spectra by multiplying the infrared spectrum by an arbitrary constant assuming continuity of the spectrum. The arbitrary constant is necessary because the calibration in the infrared region is only relative. The calibration enables the set of spectrometers in the forward view to cover globally the 500–2500 nm spectral range.

III. EXPERIMENTAL RESULTS AND DISCUSSION

Experimental results were collected in FTU (major radius R = 0.935 m, minor radius a = 0.3 m, and toroidal magnetic field B_{tor} = 2–8 T), in different scenarios and operating conditions, including RE generation and suppression,[22] during the 2015, 2016, and 2017 experimental campaigns. The REIS was installed in port 6 (Fig. 5) on the equatorial plane at z = 0 cm and at a distance of approximately 35 cm from the vacuum vessel axis. As a representative case, data and corresponding analysis are discussed here in detail for pulse No. 41899 (B_t = 5.5 T, I_p = 0.35 MA) from a "RE generation and suppression" scenario. The time traces of plasma current I_p, loop voltage V_{loop}, electron density, neutron, and gamma signals as well as the RE energy estimation (see below for details) are presented in Fig. 11. REs are generated in the current ramp-up phase, as indicated by the difference between the time traces of the NE213 scintillator (sensitive to gamma and neutrons) and BF_3 proportional counter (sensitive to neutrons only). A deuterium pellet is injected at t = 0.152 s (red spike in Fig. 11), and just after the onset of the RE plateau, at t = 0.260 s, a molybdenum impurity is injected via laser blow-off (orange spike in Fig. 11). Two more deuterium pellets (at t = 0.479 s and t = 0.548 s) increase the density of the plasma, and a substantial suppression of the RE beam is finally achieved (t > 0.5 s) as demonstrated by the neutron and gamma signals.

Synchrotron emission spectra and visible images from the REIS are presented in Figs. 12 and 13. The analysis of both images and spectra shows the large difference in signal magnitude in backward and forward views (see the time slice at 0.35 s, for example) demonstrating that the detected radiation from the forward view is indeed synchrotron emission from in-flight REs and that the effect of wall reflections is negligible. A bright spot appears in the right part of the images (corresponding to the forward view) and, correspondingly, spectra measured in the forward view vary in time, following
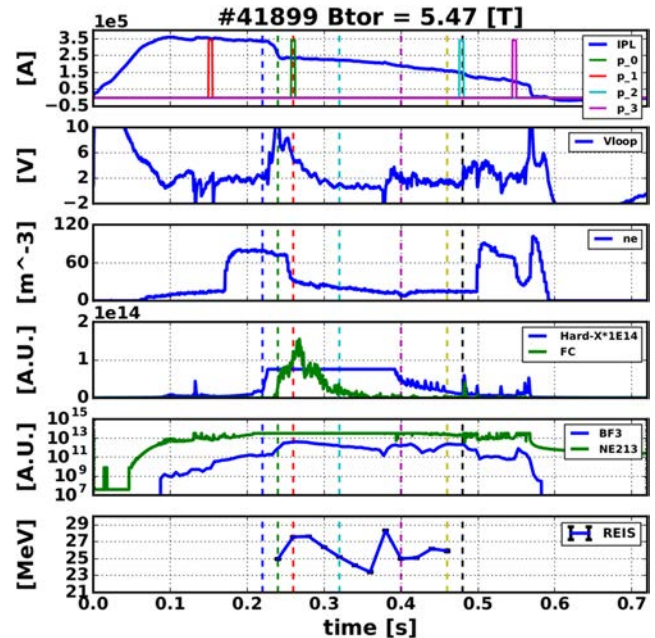

FIG. 11. FTU pulse No. 41899. From the top, time traces of the plasma current I_p, loop voltage V_{loop}, evolution of HXR monitor and fission chamber FC, NE213 scintillator (green line) and neutrons from BF_3 (blue line), and evolution of the energy fit parameter obtained from the REIS spectra between 240 ms and 480 ms.
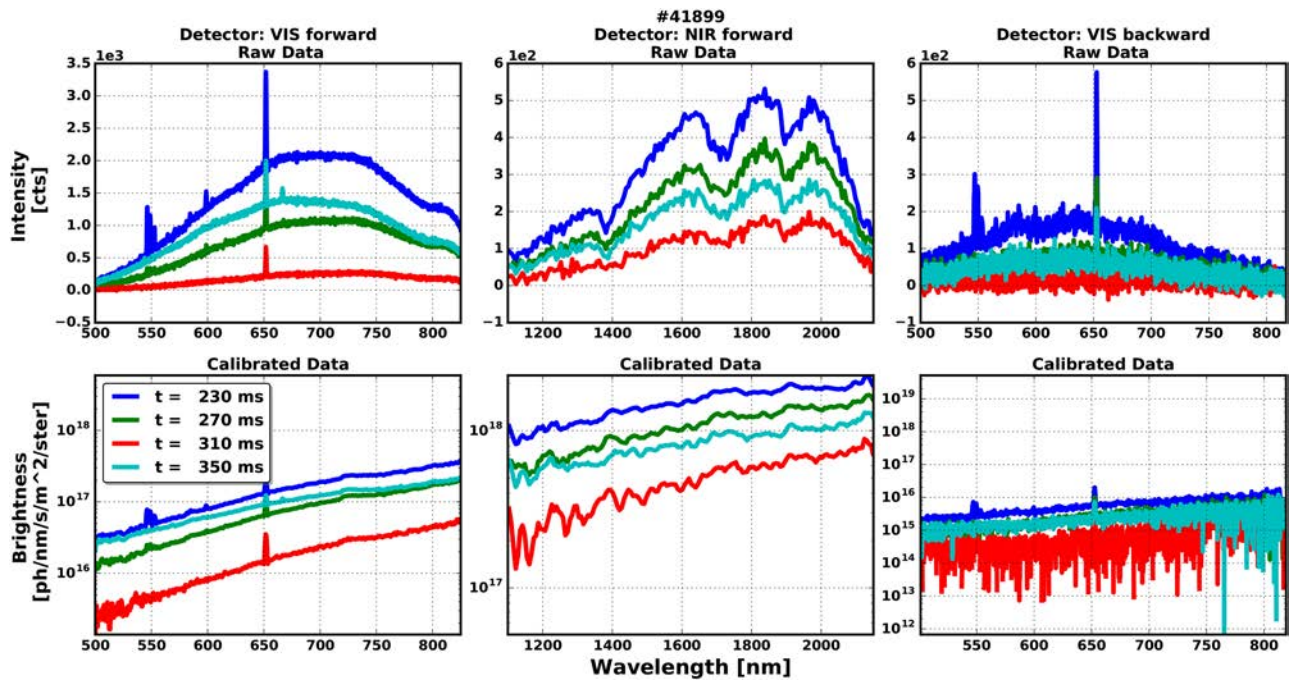
FIG. 12. Synchrotron emission radiation spectra in several time slices (pulse No. 41899), from forward (left and middle panels, for the visible and infrared parts of the spectrum, respectively) and backward (right panels) views. The raw count data with background subtraction, expressed as counts per second (cts), are in the top panels, and the corresponding relative calibrated spectra, in logarithmic scale, are in the lowers panels.

the dynamics of the RE beam, while in the backward view, they are negligible in intensity (more than two orders of magnitude lower). Similar features were observed in DIII-D.[19] Note the overexposure of the CCD camera due to the high intensity of the signal during the early phase of the RE plateau.

The RE energy is estimated from the measured spectra using Eq. (1), assuming a monoenergetic distribution and $\theta = 0.1$ rad. Several spectra have been analyzed at different times (indicated by dashed lines in Fig. 11) in the discharge. The measured spectra are calibrated, filtered using a Savitzky-Golay filter, and finally cleaned from the emission lines from plasma impurities. The best-fit total momentum p parameter is obtained for each measured spectrum.

Restricted spectral regions corresponding to the regions of minimum uncertainty on the calibration (namely, 500–830 nm and 1480–2000 nm) are used for the energy estimation. The resulting fitted spectra (black dashed lines) are presented in Fig. 14. It is not possible to apply this analysis procedure to estimate the energy from the spectrum at t < 240 ms and t > 460 ms because of the too low signal to noise ratio. From the RE beam energy estimation using the procedure described above, it is found that after the onset of the RE plateau, at t = 0.27 s, the RE energy reaches 27 MeV and then decreases gradually down to 23 MeV until a sudden rise occurring at 0.380 ms, in correspondence with a loop voltage spike.
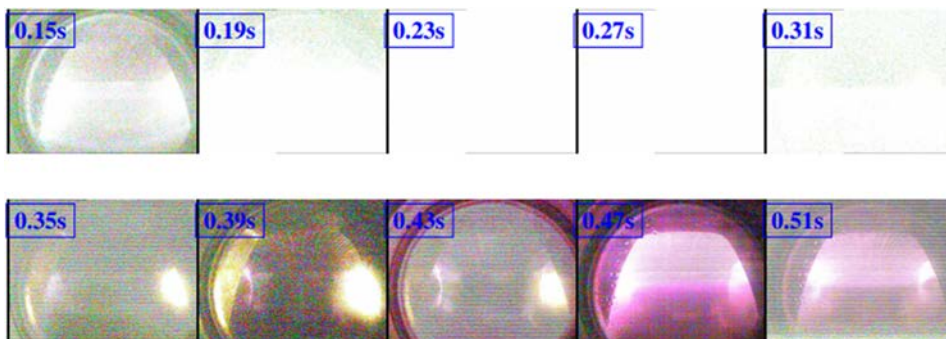

FIG. 13. Images of the synchrotron radiation captured by the REIS camera (installed on upper port 6) every 40 ms (pulse No. 41899).
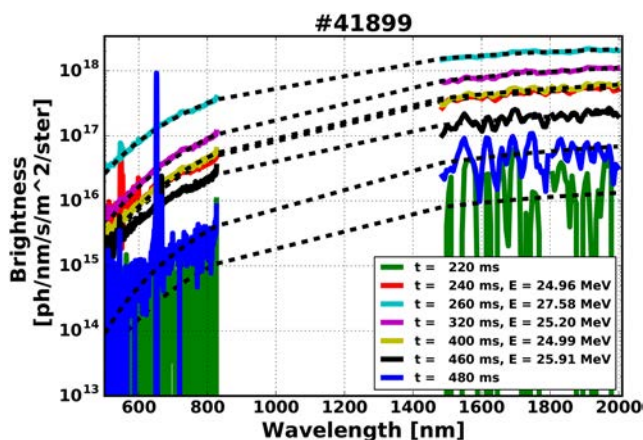
FIG. 14. Calibrated synchrotron radiation spectra (solid curves) and fitted spectra (dashed) calculated for a monoenergetic distribution and $\theta = 0.1$ (pulse No. 41899).

IV. CONCLUSION

The REIS is a new portable synchrotron radiation diagnostic developed to study in-flight REs through the measurement of visible/infrared spectra and visible images and designed to be portable for use in present medium sized-tokamaks. The main features of the REIS hardware and software as well as the calibration procedure have been described. An update of the REIS system is under way to extend the wavelength range to 5000 nm for a better coverage of the RE synchrotron emission spectrum to improve the data interpretation capability and to permit, where possible, the detection of the emission peak.

REFERENCES

[1] M. Forster, K. H. Finken, M. Lehnen, O. Willi, and Y. Xu, "Measurements of the runaway electron energy during disruptions in the tokamak TEXTOR," Phys. Plasmas **19**, 052506 (2012).

[2] K. Finken, J. Watkins, D. Rusbüldt, W. Corbett, K. Dippel, D. Goebel, and R. Moyer, "Observation of infrared synchrotron radiation from tokamak runaway electrons in TEXTOR," Nucl. Fusion **30**, 859 (1990).

[3] E. Hollmann, M. Austin, J. Boedo, N. Brooks, N. Commaux, N. Eidietis, D. Humphreys, V. Izzo, A. James, T. Jernigan et al., "Control and dissipation of runaway electron beams created during rapid shutdown experiments in DIII-D," Nucl. Fusion **53**, 083004 (2013).

[4] C. Paz-Soldan, N. W. Eidietis, R. Granetz, E. M. Hollmann, R. A. Moyer, J. C. Wesley, J. Zhang, M. E. Austin, N. A. Crocker, A. Wingen et al.,

"Growth and decay of runaway electrons above the critical electric field under quiescent conditions," Phys. Plasmas **21**, 022514 (2014).

[5] O. Tudisco, G. M. Apruzzese, P. Buratti, L. Cantarini, A. Canton, L. Carraro, V. Cocilovo, R. de Angelis, M. de Benedetti, B. Esposito, L. Gabellieri, E. Giovannozzi, G. Granucci, L. A. Grosso, G. Grosso, P. Innocente, H. Kroegler, M. Leigheb, G. Monari, D. Pacella, L. Panaccione, L. Pericoli-Ridolfini, G. Pizzicaroli, S. Podda, M. E. Puiatti, G. Rocchi, A. Sibio, A. Simonetto, P. Smeulders, U. Tartari, N. Tartoni, B. Tilia, M. Valisa, V. Zanza, and M. Zerbini, "Chapter 8: The diagnostic systems in the FTU," Fusion Sci. Technol. **45**, 402–421 (2004).

[6] B. Esposito, L. Boncagni, P. Buratti, D. Carnevale, F. Causa, M. Gospodarczyk, J. Martin-Solis, Z. Popovic, M. Agostini, G. Apruzzese, W. Bin, C. Cianfarani, R. D. Angelis, G. Granucci, A. Grosso, G. Maddaluno, D. Marocco, V. Piergotti, A. Pensa, S. Podda, G. Pucella, G. Ramogida, G. Rocchi, M. Riva, A. Sibio, C. Sozzi, B. Tilia, O. Tudisco, M. Valisa, and F. Team, "Runaway electron generation and control," Plasma Phys. Controlled Fusion **59**, 014044 (2017).

[7] D. Carnevale, B. Esposito, M. Gospodarczyk, Z. Popovic et al., "Analysis of runaway beam suppression experiments in FTU," in preprint EUROFUSION WPMST2-CP(16) 15186, paper EX/P8-22, 2016 IAEA Fusion Energy Conference, 2016.

[8] B. Esposito, J. R. Martín-Solís, F. M. Poli, J. A. Mier, R. Sánchez, and L. Panaccione, "Dynamics of high energy runaway electrons in the frascati tokamak upgrade," Phys. Plasmas **10**, 2350–2360 (2003).

[9] G. Pucella, E. Alessi, L. Amicucci, B. Angelini, M. Apicella, G. Apruzzese, G. Artaserse, F. Belli, W. Bin, L. Boncagni et al., "Overview of the FTU results," Nucl. Fusion **57**, 102004 (2017).

[10] M. Gospodarczyk, A. Gabrielli, D. Carnevale, L. Boncagni, G. Ferró, B. Esposito, M. Sassano, F. Martinelli, S. Galeani, and Z. Popovic, "Control-oriented model of disruption generated RE beam at FTU," Fusion Eng. Des. **135**, 42–49 (2018).

[11] R. Jaspers, N. J. Lopes Cardozo, A. J. Donné, H. L. Widdershoven, and K. H. Finken, "A synchrotron radiation diagnostic to observe relativistic runaway electrons in a tokamak plasma," Rev. Sci. Instrum. **72**, 466–470 (2001).

[12] R. Tinguely et al., "Spatiotemporal evolution of runaway electrons from synchrotron images in Alcator C-Mod," Plasma Phys. Controlled Fusion **60**, 124001 (2018).

[13] K. Wongrach, K. H. Finken, S. S. Abdullaev, R. Koslowski, O. Willi, and L. Zeng, "Measurement of synchrotron radiation from runaway electrons during the TEXTOR tokamak disruptions," Nucl. Fusion **54**, 043011 (2014).

[14] R. H. Tong, Z. Y. Chen, M. Zhang, D. W. Huang, W. Yan, and G. Zhuang, "Observation of runaway electrons by infrared camera in J-TEXT," Rev. Sci. Instrum. **87**, 11E113 (2016).

[15] M. Vlainic, J. Mlynar, J. Cavalier, V. Weinzettl, R. Paprok, M. Imrisek, O. Ficker, M. Varavin, P. Vondracek, and J. M. Noterdaeme, "Post-disruptive runaway electron beams in the COMPASS tokamak," J. Plasma Phys. **81**, 475810506 (2015); e-print arXiv:1503.02947.

[16] R. J. Zhou, L. Q. Hu, E. Z. Li, M. Xu, G. Q. Zhong, L. Q. Xu, S. Y. Lin, and J. Z. Zhang, "Investigation of ring-like runaway electron beams in the EAST tokamak," Plasma Phys. Controlled Fusion **55**, 055006 (2013).

[17] M. Cheon, J. Kim, Y. An, D. Seo, and H. Kim, "Observation of the loss of pre-disruptive runaway electrons in KSTAR ohmic plasma disruptions," Nucl. Fusion **56**, 126004 (2016).

[18] G. Papp, G. Pautasso, J. Decker, M. Gobbin, P. J. Mccarthy, P. Blanchard, D. Carnevale, D. Choi, S. Coda, B. Duval, R. Dux, B. Esposito, O. Ficker, R. Fischer, C. Fuchs, C. Galperti, L. Giannone, A. Gude, B. Labit, K. Lackner, T. Lunt, L. Marelli, P. Martin, A. Mlynek, E. Nardon, M. Maraschek, P. Marmillod, M. Nocente, Y. Peysson, P. Piovesan, V. V. Plyusnin, G. I. Pokol, S. Potzel, C. Reux, O. Sauter, B. Sieglin, U. Sheikh, C. Sommariva, W. Suttrop, G. Tardini, M. Teschke, D. Testa, W. Treutterer, M. Valisa, S. P. Centre, C. Republic, U. D. Lisboa, and C. R. Frascati, "Runaway electron generation and mitigation on the European medium sized tokamaks ASDEX Upgrade and TCV ASDEX Upgrade runaway scenario," in Proceedings of 2016 IAEA Fusion Energy Conference (IAEA, 2016), pp. 1–8.

[19] J. Yu, E. Hollmann, N. Commaux, N. Eidietis, D. Humphreys, A. James, T. C. Jernigan, and R. Moyer, "Visible imaging and spectroscopy of disruption runaway electrons in DIII-D," Phys. Plasmas **20**, 042113 (2013).

[20]A. Stahl, O. Embréus, G. Papp, M. Landreman, and T. Fülöp, "Kinetic modelling of runaway electrons in dynamic scenarios," Nucl. Fusion **56**, 112009 (2016).

[21]A. Stahl, M. Landreman, G. Papp, E. Hollmann, and T. Fülöp, "Synchrotron radiation from a runaway electron distribution in tokamaks," Phys. Plasmas **20**, 093302 (2013).

[22]Z. Popovic, B. Esposito, J. Marton-Solis, W. Bin, P. Buratti, D. Carnevale, F. Causa, M. Gospodarczyk, D. Marocco, G. Ramogida *et al.*, "On the measurement of the threshold electric field for runaway electron generation in the frascati tokamak upgrade," Phys. Plasmas **23**, 122501 (2016).